Precursor for wind reversal in a square Rayleigh-Bénard cell

Bérengère Podvin[1,*] and Anne Sergent[1,2]
[1]*CNRS, LIMSI, UPR3251, BP 133, 91403 Orsay Cedex, Université Paris-Saclay, France*
[2]*Universite Pierre et Marie Curie-Paris 6, 4 Place Jussieu, 75252 Paris, Cedex 05, France*
(Received 8 April 2016; published 26 January 2017)

We investigate large-scale circulation reversals in a two-dimensional Rayleigh-Bénard cell using a proper orthogonal decomposition (POD)-based, five-mode model. The Rayleigh number considered is $\mathrm{Ra} = 5 \times 10^7$ and the Prandtl number is $\mathrm{Pr} = 4.3$. A precursor event, corresponding to the action of a mode L_* which disconnects the core region from the boundary layers before the onset of the reversal, is identified in the simulation. The five-mode model predicts correctly the behavior of the POD modes observed in the simulation, and in particular that of mode L_*. The presence of mode L_*, which was not included in an earlier, lower-dimensional version of the model [Podvin and Sergent, J. Fluid Mech. **766**, 172 (2015)], is found to be instrumental for the reversal dynamics of the model, which suggests that it may also be important for those of the simulation. Reversals can therefore be characterized by three time scales: the transition duration, the interreversal time, and the precursor duration, which separates the precursor event from the onset of the reversal. The distribution of the time scales is found to agree well with the simulation when small-scale intermittency is taken into account through the introduction of noise in the model coefficients.

DOI: 10.1103/PhysRevE.95.013112

I. INTRODUCTION

Many physical systems are characterized by intermittent dynamics where the flow settles down for long periods of times near different quasistationary states separated by rapid, violent excursions. A well-known geophysical example is the Earth's magnetic field which has reversed its polarity several times throughout its history. Similar reversals have been reproduced in magnetohydrodynamic experiments [1]. Another example of multistability can be found in aerodynamics, where the recirculation flow behind a bluff body, such as an automobile, shifts over long time scales between two symmetry-breaking positions, while the averaged flow corresponds to a statistically symmetric wake [2]. In Rayleigh-Bénard convection, thermal fluctuations organize themselves into large-scale rolls which change orientation in an intermittent fashion [3,4]. In cylindrical cells, the main axis of the roll can drift slowly but radical reorientations can also occur in an intermittent fashion. These reorientations can be led by rotations of the main circulation or cessations (suppression of the main circulation) [5]. In two-dimensional (2D) or nearly 2D domains, reversals of the large-scale circulation can also take place [6,7]. In addition, the large-scale circulation sometimes disappears and is replaced temporarily by a two-roll mode, which creates a cessationlike event [6].

A long-standing question is the origin of the reversal. The physical mechanism identified so far involves the development of corner flows, which are observed to grow during reversals [3,8]. Reversals can be interpreted as the consequence of a thermal imbalance in the cell [9], and their initiation is therefore dependent on the dynamics of small-scale thermal plumes, which form in the horizontal boundary layers at small scales and are transported into the bulk. We note that the influence of small scales remains essential even in the absence of thermal convection: reversals in a 2D cell were found to be connected to the development of vortex filaments along the walls [10]. Alternatively, reversals can be seen as a large-scale restoration process of the statistical symmetry of the flow: while instantaneous realizations of the turbulent flow are not symmetric, the assumption of ergodicity requires that the flow trajectory in phase space should be symmetric [11]. One question is then to determine if and how large-scale symmetry breaking occurs during reversals.

Different approaches have led to a wide diversity of models that describe reversals. Araujo *et al.* [12] have computed the force and thermal balance on a single plume detached from the boundary layer and have derived from it a nonlinear set of equations, which is similar to Lorenz's model and exhibits deterministic chaotic reversals. However, many approaches rely on models where the turbulent background fluctuations are represented by stochastic noise. Sreenivasan *et al.* [9] relied on the concept of metastable states separated by an energy barrier to describe the physics. Benzi [13] used an energy cascade model that reproduced some statistical properties of the Navier-Stokes equations. Another example is the model of Brown and Ahlers [5,14], which is based on the strength and the orientation of the large-scale circulation. Recent versions of the model can take into account the influence of the geometry [15].

All these models are based on physical modeling of varying complexity and rely on fundamental assumptions about the dominant patterns of the flow. In contrast, proper orthogonal decomposition (POD) provides an unbiased framework which extracts spatial modes from the data using an energy-based criterion. POD modes can be compared with other classical decompositions such as Fourier modes [6,16,17]. In addition, for a given set of POD modes, one can derive a model from projection of the Navier-Stokes equations that predicts the temporal evolution of the amplitudes of the modes. Since POD modes constitute an orthogonal, hierarchically ordered (in the energy sense) basis, the projection of the field onto these modes converges towards the full field as the number of modes increases, and the dynamics of the model is expected to converge towards those of the Navier-Stokes equations if

*Corresponding author: podvin@limsi.fr

the truncation is large enough. However, it is not possible to determine *a priori* how many modes are necessary to capture the dynamics of the flow.

As pointed out by Rempfer [18], the restriction to a low-dimensional basis can affect the domain of validity of the model, as only a partial view of the full dynamics is provided. We emphasize that the connection between the mathematical predictions of models and the physical processes they describe is not one to one, as (i) POD modes do not unequivocally correspond to physics-based coherent structures (see the discussion in [19]), and (ii) the details of the interaction scenario representing a given physical mechanism depend on the POD modes selected in the truncation.

Reversals were recently investigated in a paper using proper orthogonal decomposition (POD) [8]. A description of the large-scale reversal process was provided by a model based on the three most energetic POD modes. A good agreement was observed with experimental and numerical studies [6,20,21]. It was shown that reversals in the three-mode model were associated with the instability of a two-cell, symmetry-breaking mode. The model reproduced reversals and cessations observed in the Direct Numerical Simulation (DNS) under the condition that noise was added to the model.

In the present paper we consider two additional POD modes. A scenario for reversals is presented: it involves as a key player one of these extra modes, which controls the transfer between the core region and the boundary layer and precedes the reversal. The paper is organized as follows: we first present the numerical configuration, then detail the behavior of POD modes in the simulation. A comparison of the latter with the predictions of the POD-based model is provided. We show that the model predicts regular reversals in the absence of noise and in the absence of symmetry-breaking modes. The influence of symmetry-breaking modes and noise on the time scales of the reversals is then examined.

II. CONFIGURATION

A. Equations of motion

The configuration is similar to that used in [8]. The domain is a 2D square filled with water ($\mathrm{Pr} = \nu/\kappa = 4.3$), heated at the bottom and cooled at the top. The flow is characterized by the Rayleigh number

$$\mathrm{Ra} = \frac{\tilde{\alpha} g \Delta T h^3}{\nu \kappa},$$

where $\tilde{\alpha}$ is the volumetric thermal expansion coefficient, g is the gravity, ΔT is the temperature difference between both isothermal horizontal plates, h is the height between the horizontal plates, and ν and κ are respectively the fluid kinematic viscosity and thermal diffusivity. The Rayleigh number in the study is set to $\mathrm{Ra} = 5 \times 10^7$, which corresponds to a flow regime where intermittency is expected [20].

The flow equations are based on the Boussinesq approximation. The reference length and velocity units used to make the equations nondimensional are the height between the plates h and the velocity $\frac{\kappa}{h}\sqrt{\mathrm{Ra}}$. The temperature is made dimensionless with ΔT. The horizontal and vertical directions will respectively be labeled x and z. If $\underline{u}$ is the velocity vector [$\underline{u} = (u,w)$] and θ is the dimensionless temperature, then the equations based on the nondimensional reference units are

$$\nabla \cdot \underline{u} = 0, \tag{1}$$

$$\frac{\partial u}{\partial t} + u\frac{\partial u}{\partial x} + w\frac{\partial u}{\partial z} = -\frac{\partial p}{\partial x} + \frac{\mathrm{Pr}}{\mathrm{Ra}^{1/2}}\Delta u, \tag{2}$$

$$\frac{\partial w}{\partial t} + u\frac{\partial w}{\partial x} + w\frac{\partial w}{\partial z} = -\frac{\partial p}{\partial z} + \frac{Pr}{\mathrm{Ra}^{1/2}}\Delta w + \mathrm{Pr}\theta, \tag{3}$$

$$\frac{\partial \theta}{\partial t} + u\frac{\partial \theta}{\partial x} + w\frac{\partial \theta}{\partial z} = \frac{1}{\mathrm{Ra}^{1/2}}\Delta \theta. \tag{4}$$

The velocity is zero on all walls. The temperature is set to 0.5 and -0.5 respectively on the bottom and top walls. Adiabatic conditions are used on the side walls.

Taking the origin of the axes (x^*,z^*) to be set in the center of the cell, the velocity and the temperature fields obey the following statistical symmetries for the problem: (i) the reflexion symmetry S_x with respect to the vertical axis $x^* = 0$ which leaves all physical quantities invariant,

$$\begin{bmatrix} u \\ w \\ \theta \end{bmatrix}(x^*,z^*) \rightarrow \begin{bmatrix} -u \\ w \\ \theta \end{bmatrix}(-x^*,z^*);$$

(ii) the reflexion symmetry S_z with respect to the horizontal axis $z^* = 0$ which leaves the velocity invariant and transforms the temperature variation into its opposite,

$$\begin{bmatrix} u \\ w \\ \theta \end{bmatrix}(x^*,z^*) \rightarrow \begin{bmatrix} u \\ -w \\ -\theta \end{bmatrix}(x^*,-z^*);$$

(iii) the centrosymmetry or rotation of origin of the cell center $(x^*,z^*) = (0,0)$ $R_\pi = S_x \circ S_z = S_z \circ S_x$,

$$\begin{bmatrix} u \\ w \\ \theta \end{bmatrix}(x^*,z^*) \rightarrow \begin{bmatrix} -u \\ -w \\ -\theta \end{bmatrix}(-x^*,-z^*).$$

Along with the identity, this forms a four-dimensional symmetry group.

In the paper we will refer to a mode as symmetry breaking if it is not centrosymmetric with respect to R_π. We note that if a mode is symmetric or antisymmetric with respect to both S_x and S_z then it is centrosymmetric with respect to R_π. However if is symmetric with respect to one and antisymmetric with respect to the other, then the symmetry is broken.

B. Numerical method

The simulations are carried out with a multidomain spectral code. Spectral collocation is used for spatial discretization. Details of the method can be found in [22]. The domain decomposition in the horizontal direction x is carried out by the Schur complement method and implemented with the MPI library. Chebyshev modes are used in all directions. We use 384 points or polynomials in the horizontal direction and 158 points in the vertical direction.

Time integration of the governing equations (1)–(4) is performed through a second-order semi-implicit scheme. It combines a second-order backward Euler scheme with an implicit treatment for the diffusion terms and an explicit second-order Adams-Bashforth extrapolation for the nonlinear

terms. The time step is equal to 0.0006 convective time unit. Incompressibility is imposed by a projection method which retains second-order accuracy of the time integration. The code has been validated and verified for resolution [8].

III. PROPER ORTHOGONAL DECOMPOSITION

A. Definition

The approach used to derive the POD-based model has been described in [8]. Proper orthogonal decomposition ([19]) consists of decomposing the flow variables $\underline{q}$ as a superposition of spatial structures or empirical eigenfunctions $\underline{\phi}(\underline{x})$ whose amplitude varies in time, which means that

$$\underline{q}(\underline{x},t) = \sum_{n=1}^{\infty} a^n(t)\underline{\phi}_{\underline{q}}^n(\underline{x}). \tag{5}$$

The POD modes are hierarchically organized according to their energies $\lambda_1 > \lambda_2 > \ldots \lambda_n$. The spatial eigenfunctions are orthogonal. If the empirical eigenfunctions are normalized, we have $\langle a^n(t)a^m(t)\rangle = \delta_{nm}\lambda_n$ where δ_{nm} is the Kronecker symbol and $\langle\ \rangle$ is a time average. More details can be found in [19].

We use a joint velocity and temperature decomposition, with a rescaling factor of 1 for the temperature.

To carry out the proper orthogonal decomposition of a set of variables $\underline{q}$, one solves the following eigenvalue problem:

$$\int \langle \underline{q}(\underline{x},t)\underline{q}(\underline{x}',t)\rangle \underline{\phi}_{\underline{q}}(\underline{x}')d\underline{x}' = \lambda \underline{\phi}_{\underline{q}}(\underline{x}), \tag{6}$$

where $\langle \underline{q}(\underline{x},t)\underline{q}(\underline{x}',t)\rangle$ is the spatial autocorrelation tensor. The spatial autocorrelation tensor is computed from N individual snapshots obtained at instants t_n, $\underline{q}(\underline{x},t_n)$:

$$\langle \underline{q}(\underline{x},t)\underline{q}(\underline{x}',t)\rangle = \frac{1}{N}\sum_{n=1}^{N} \underline{q}(\underline{x},t_n)\underline{q}(\underline{x}',t_n).$$

Due to the size of the physical grid, $O(50\,000)$, the method of snapshots [23] was used to extract empirical eigenfunctions. The method of snapshots [23] is based on the fact that the eigenfunctions can be written as the linear combination of these N snapshots,

$$\underline{\phi}_{\underline{q}}^n(\underline{x}) = A_p^n \underline{q}(\underline{x},t_p), \tag{7}$$

to rewrite the eigenvalue problem. One can show that A_p^n represents the temporal amplitude of the mode $\underline{\phi}^n$ at time t_p, i.e.,

$$A_p^n = a^n(t_p). \tag{8}$$

The set of snapshots consisted exclusively of realizations extracted from the simulation (no additional symmetry was applied to the set).

TABLE I. Eigenvalues and symmetries obeyed by the POD modes.

Mode index	λ^n	S_x	S_z
1	1.1	antisymmetric	antisymmetric
2	0.26	symmetric	symmetric
3	0.18	symmetric	antisymmetric (velocity)
4	0.06	antisymmetric	antisymmetric
5	0.05	antisymmetric (velocity)	symmetric

B. Spatial eigenfunctions

Proper orthogonal decomposition was applied to both velocity and temperature variables. The dataset included 40% more snapshots than in [8]. The time separation between two snapshots was six time units. The eigenvalues of the five most energetic modes, which capture 90% of the joint kinetic and thermal energy, are given in Table I. The shapes of the modes can be seen in Fig. 1 and as expected are very similar to the modes obtained in [8]. For the joint velocity and temperature decomposition, the most energetic mode is a single roll (denoted L) associated with a dominant thermal flux along the middle portion of the vertical boundary

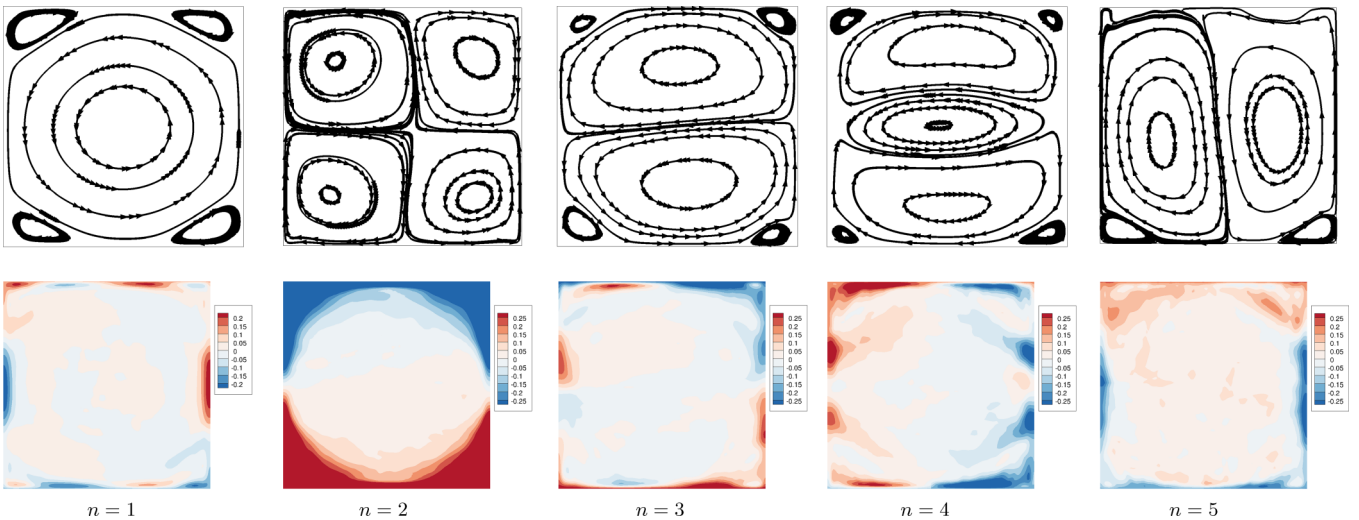

FIG. 1. POD modes for the new dataset. Top: Velocity modes. Bottom: Temperature mode isocontours at −0.2, −0.15, −0.1, 0.1, 0.15, 0.2. Dashed lines indicate negative values.

TABLE II. Linear coefficients L^d_{np} and L^b_{np} respectively corresponding to the dissipation and the buoyancy force term.

L^d_{np}	$p=1$	$p=2$	$p=3$	$p=4$	$p=5$
$m=1$	−0.28	−0.09	0.02	0.44	−0.057
$m=2$	−0.02	−1.79	0.13	0.10	−0.10
$m=3$	0.003	0.097	−0.37	−0.03	−0.03
$m=4$	0.02	0.02	−0.01	−0.78	−0.006
$m=5$	−0.0025	−0.02	−0.009	−0.004	−0.43
L^b_{np}	$p=1$	$p=2$	$p=3$	$p=4$	$p=5$
$n=1$	0.08	0.14	0.015	0.20	0.077
$n=2$	0.002	1.85	−0.185	−0.10	−0.075
$n=3$	0.0146	−0.10	0.20	−0.08	0.093
$n=4$	−0.13	−0.016	0.022	0.40	0.018
$n=5$	−0.0042	0.019	0.0198	0.006	0.38

TABLE III. Quadratic coefficients Q_{nmp}. Only the upper part of the symmetric matrix is represented. The coefficients are multiplied by a factor of 10 for reading convenience.

$10\times Q_{1mp}$	$p=1$	$p=2$	$p=3$	$p=4$	$p=5$
$m=1$	−0.0001	**6.55**	0.41	−0.04	0.069
$m=2$		−0.42	0.31	2.48	0.13
$m=3$			0.068	0.28	−0.035
$m=4$				0.15	0.15
$m=5$					0.0326
$10\times Q_{2mp}$	$p=1$	$p=2$	$p=3$	$p=4$	$p=5$
$m=1$	**−28.33**	1.84	−3.00	**−15.92**	1.23
$m=2$		−0.0097	−0.79	−0.49	0.0065
$m=3$			**−3.66**	0.92	−0.38
$m=4$				2.41	−0.92
$m=5$					0.21
$10\times Q_{3mp}$	$p=1$	$p=2$	$p=3$	$p=4$	$p=5$
$m=1$	−2.54	2.32	−0.41	−1.24	**−22.23**
$m=2$		−0.99	**5.14**	−0.99	−1.50
$m=3$			0.0001	0.26	1.26
$m=4$				0.065	**8.81**
$m=5$					0.12
$10\times Q_{4mp}$	$p=1$	$p=2$	$p=3$	$p=4$	$p=5$
$m=1$	0.82	**20.88**	−1.33	−2.59	6.17
$m=2$		−1.99	−0.84	−9.69	0.63
$m=3$			0.75	−0.19	1.89
$m=4$				−0.0005	−3.07
$m=5$					0.096
$10\times Q_{5mp}$	$p=1$	$p=2$	$p=3$	$p=4$	$p=5$
$m=1$	−1.57	−9.43	**82.28**	−11.36	−0.74
$m=2$		0.05	7.62	3.99	−1.08
$m=3$			−4.70	**-35.41**	−0.46
$m=4$				4.92	−0.12
$m=5$					−0.0007

layers. The second most energetic mode is a quadrupolar velocity mode (Q) associated with the mean temperature field, with a heat flux which is maximal in the top and bottom sections of the vertical boundary layers. The third mode is a two-roll, symmetry-breaking mode S. These three modes were examined in detail in [8].

We now consider the next two most energetic modes. The fourth mode, which consists of two corotating stacked rolls, is entirely antisymmetric with respect to S_z and S_x. The associated temperature field consists of fluctuations of opposite signs on each vertical half of the cavity, and is characterized by a strong intensity in the boundary layers, in particular close to the center section of the vertical boundary layers. The fifth mode is constituted by two vertical rolls. It appears to be symmetric with respect to S_z and antisymmetric with respect to S_x. Although the velocity field is symmetric with respect to S_x, and antisymmetric with respect to S_z, the temperature field only obeys the S_x symmetry, not the S_z symmetry: the field in the top horizontal boundary layer has an opposite sign to that in the bottom boundary layer, while it remains of constant sign along the largest part of the vertical walls. The symmetries of the different modes are summarized in Table I. We can note that modes 1, 2, and 4 have the same symmetry with respect to both reflexions, which means that they are all symmetric with respect to the central symmetry, while modes 3 and 5 have opposite symmetries, which means that the velocity field is antisymmetric with respect to the central symmetry. We therefore adopt the following notations for the modes 4 and 5: mode 4 is denoted L_* since it is fully antisymmetric like the mode L, while mode 5 is called S_* since it is a symmetry-breaking mode with opposite symmetries to the mode S for S_x and S_z (see Table I).

C. Histories

In all that follows, for clarity and whenever there is no ambiguity, we will refer to the amplitude of the nth POD mode $a^n(t)$ as a mode itself, i.e., L will refer to the temporal amplitude of the first mode a^1, Q to that of the second mode a^2, and so forth. The time histories of the POD normalized amplitudes $a^n(t)/\sqrt{\lambda_n}$ for $1 \leqslant n \leqslant 5$ were extracted from the simulation and represented in Fig. 2 over a restricted time period, chosen to illustrate representative reversals. Corresponding histograms computed over several more reversals are also included. Figure 2 shows that reversals are characterized by rapid excursions for all the POD modes. The large-scale circulation mode L switches between two nearly constant and opposite values. At the onset of reversals, the quadrupolar mode Q increases then collapses before increasing again. The two-roll mode S is nearly zero between reversals, but increases sharply with positive and negative values during reversals.

In contrast, the antisymmetric mode L_* is never close to zero for large amounts of time between reversals. This is confirmed by its distribution shown in Fig. 2(d), which is much wider than that associated with S or S_*. The mode changes sign several times during a reversal cycle. In the quasistationary state following a reversal, if L is positive, then L_* is negative (for instance at $t = 80$–130, $t = 250$–300; $t = 400$–450 in Fig. 2), which means—see Fig. 1—that the mode tends to decelerate the center of the roll and accelerate the flow in its outer part. At least one sign change of L_* was observed before every reversal. The change occurred on the order of several O(10) convective units before the collapse of mode L, i.e.,

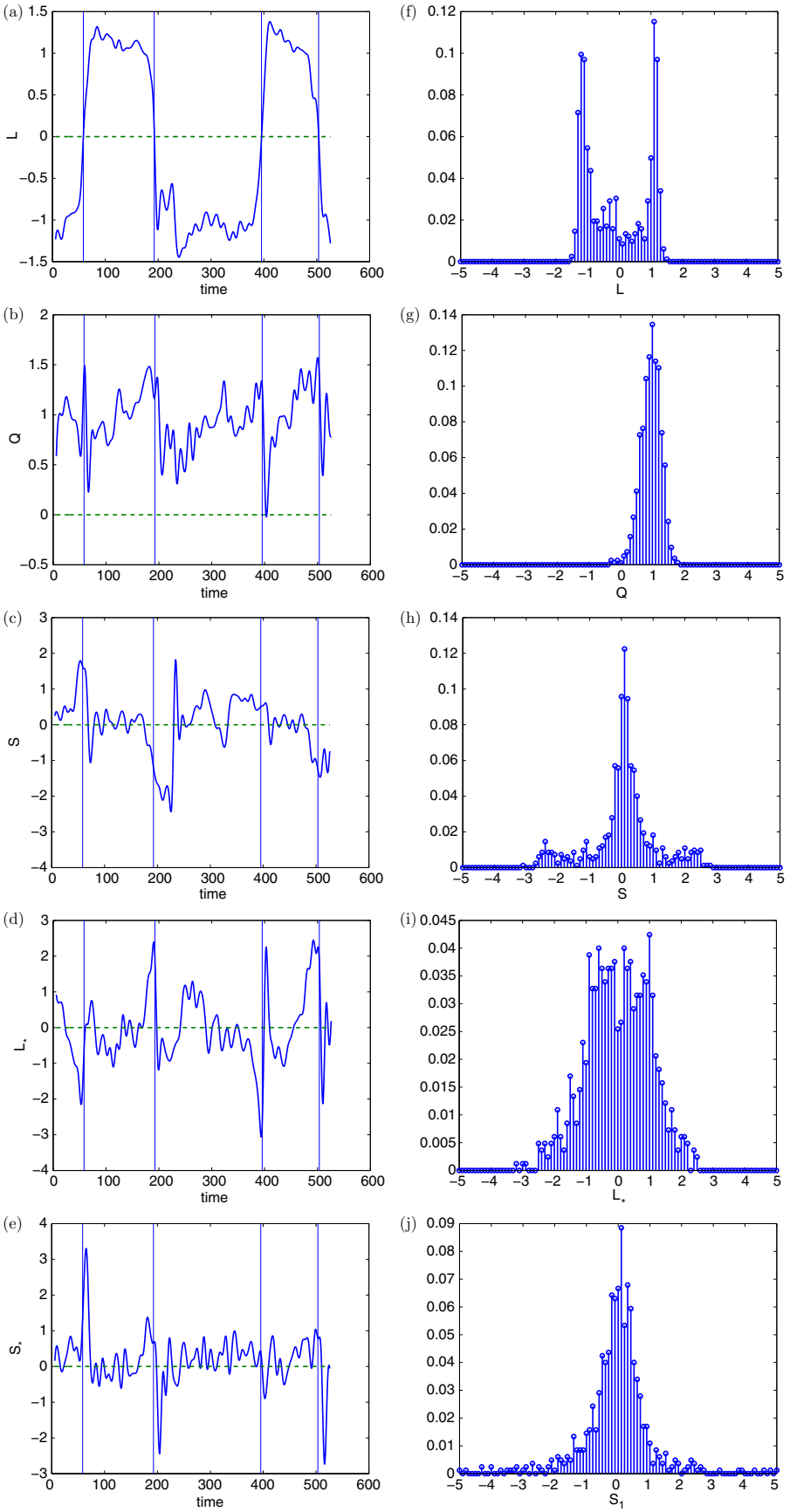

FIG. 2. Behavior of the normalized POD amplitudes $a^n/\sqrt{\lambda_n}$ during reversals. Left: time evolution. Right: histograms computed over a longer time sequence: (a) and (f) $n = 1(L)$; (b) and (g) $n = 2(Q)$; (c) and (h) $n = 3(S)$; (d) and (i) $n = 4(L_*)$; (e) and (j) $n = 5(S_*)$.

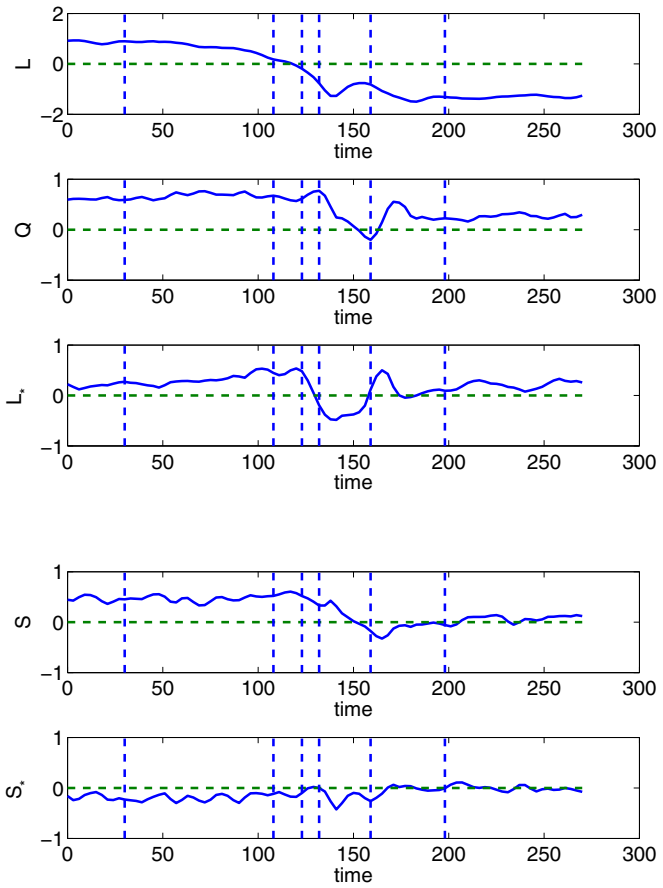

FIG. 3. Evolution of the POD coefficients during a reversal event.

before the reversal took place. This sign change means that the boundary layer wind decreases, while the flow is accelerated in the bulk. However, this motion cannot be self-sustained as the flow tends to be well mixed in the bulk: the large-scale circulation is sustained by the transport of thermal plumes originating from the horizontal boundary layers and driven into the bulk by the shear layer. The intensity of mode L_* remains strong until L goes through zero. At least two or more sign changes are observed again for the mode L_* before it settles down towards a positive value as L is now negative. In the next section we will show how the model is able to reproduce the dynamics of L and L_* observed in the simulation.

The S_* mode behaves in a very similar manner to the mode S: it is also nearly zero between reversals, and experiences sharp excursions during reversals. We can therefore propose the following description of the simulation:

(i) Between reversals: mode L is constant, mode Q is positive, and mode L_* is nonzero (L_* is negative when L is positive immediately following a reversal), while modes S and S_* are close to zero. The variations of all modes are small, except those of mode L_* which changes sign at least once. This indicates that some large-scale changes do take place between reversals. The first sign change of L_* is taken to constitute a precursor of the reversal.

(ii) During reversals: mode L collapses, while mode Q increases and modes L_*, S, and S_* experience sharp excursions. Mode L_* then changes sign several times while mode Q decreases then increases again.

The evolution of the POD coefficients during a single reversal event is represented in Fig. 3. The time origin is arbitrary and corresponds to a moment preceding a reversal (i.e., L_* has already changed sign and has the same sign as L). The corresponding instantaneous velocity field and temperature field are shown in Fig. 5 at the times corresponding to the dashed vertical lines in Fig. 3. These times respectively correspond to (i) a positive value of L_*, (ii) a maximum of L_*, (iii) a zero of L, (iv) a maximum of Q, (v) a minimum of Q, and (vi) an return to a quasistationary state.

As expected, the flow before the reversal at $t = 30$ is constituted by a main roll along with two corner vortices. The corner vortices grow, squeezing the main vortex in its middle part at $t = 112$, and pinching it into two vortices at $t = 123$, yielding a quadrupolar flow. The flow gives way through vortex reconnection to a main roll (see $t = 135$) which will eventually reorient around the diagonal opposite the initial state (see $t = 162$). At $t = 201$, the flow is relaxing towards the new quasistationary state. This description is similar to what was proposed by [20] and can be connected to the Fourier-based approach proposed by [6].

To show that the single reversal event selected from the DNS represents typical behavior, we represented in Fig. 4 the phase portraits in the L, L_* space. We represented in Fig. 4(a) the trajectories corresponding to the transition times, which

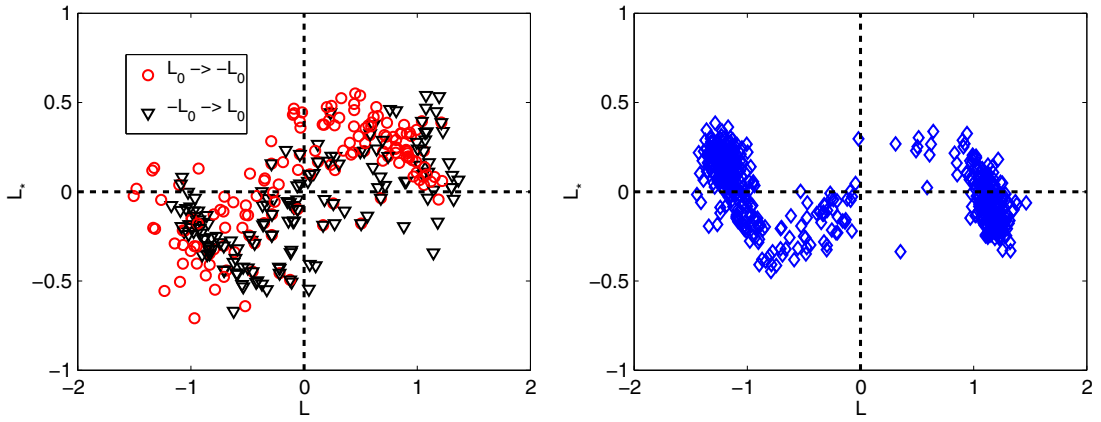

FIG. 4. Phase portraits of the POD coefficients in the $(L, L_*$ space (a) during the transitions, (b) outside the transitions.

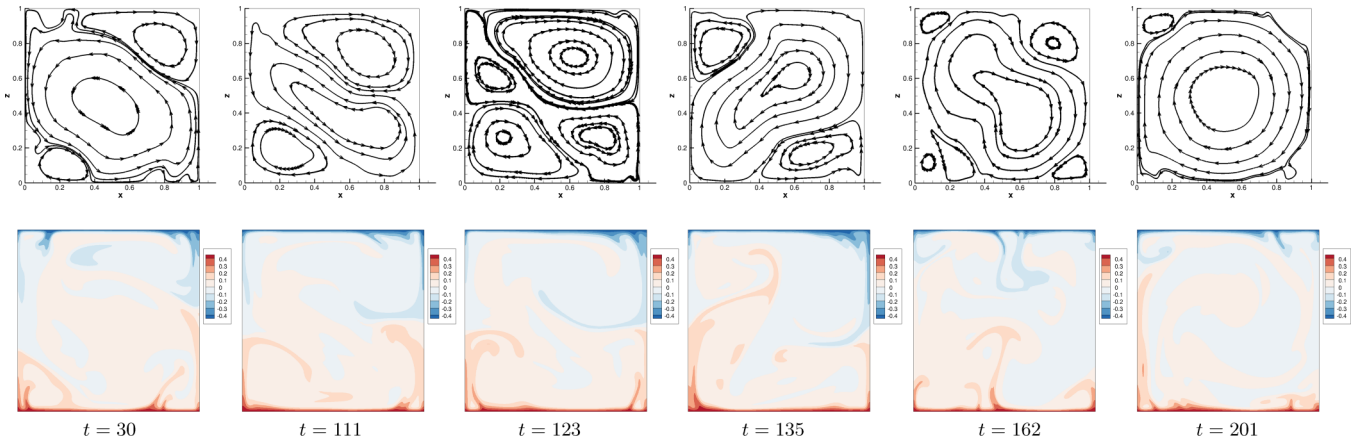

FIG. 5. Velocity and temperature field during a reversal event at selected times indicated in Fig. 3. Top: velocity streamlines. Bottom: temperature contours 0.2, 0.15, 0.1, −0.1, −0.15, −0.2 (dashed lines indicate negative values).

were defined as time intervals of the form $[t_r - \Delta t, t_r + \Delta t]$, where t_r corresponds to a crossing of the $L = 0$ axis and Δt is taken to be large enough to capture most of the transitions (for the figure, we took $\Delta t = 18$, which is slightly larger than the average transition duration of 16 time units as will be seen in the Sec. IV D). One can see that the quadrants $LL_* > 0$ are predominantly occupied during the transitions. Moreover, a distinction was made between the transitions from positive to negative L and from negative to positive L, and it can be seen that each type of transition occupies a well-defined portion of phase space: $L_* < 0$ when L crosses the zero axis from left to right (negative to positive) and $L_* > 0$ when the switch is from positive to negative values. This is in agreement with the scenario proposed above. The phase portraits at times other than these transition times are represented in Fig. 4(b). The flow spends most of these times near the quasi-steady state $|L| = 1$. Following a transition, the flow state is located in the quadrant space $LL_* < 0$ however one can see that after some time (but still well before a new reversal has occurred) the mode L_* crosses the axis and the state moves to the quadrant $LL_* > 0$. At least one axis crossing of L_* outside the transitions was observed before each reversal - in 80% of the reversals L_* crossed the axis only once. This constitutes the precursor event of reversals.

D. Adequacy of the large-scale description during reversals

The fields shown in Fig. 5 were projected onto the first five POD modes and are represented in Fig. 6. Comparing Figs. 5 and 6 allows us to evaluate the capacity of the POD modes to represent the phenomena taking place during reversals. The POD focuses mostly on the large-scale field, leaving out small-scale components. This means that the projection fails to capture individual ejections of thermal plumes into the bulk, as can be seen by comparing the bottom rows of Figs. 5 and 6. The orientation of the roll can be inferred from the relative height of the temperature contours, but details of the temperature field within the bulk are absent.

In contrast, the velocity field in Fig. 6 shows similarities with Fig. 5 and confirms the scenario proposed in Sec. III C: the quadrupolar flow is clearly apparent in the projection at $t = 111$ and $t = 123$. We note that, after the reversal, the flow does not settle immediately into the symmetric state. At $t = 162$ the main roll appears to be oriented along the "wrong" diagonal (i.e., the one opposite to that corresponding to the quasistationary state). At this time the projected temperature field consists of cold fluid in the bottom and hot fluid in the top boundary layers, which is in opposition to the DNS field in the boundary layers (compare Figs. 5 and 6 at $t = 162$). This temperature inversion reflects the fact that cold and hot

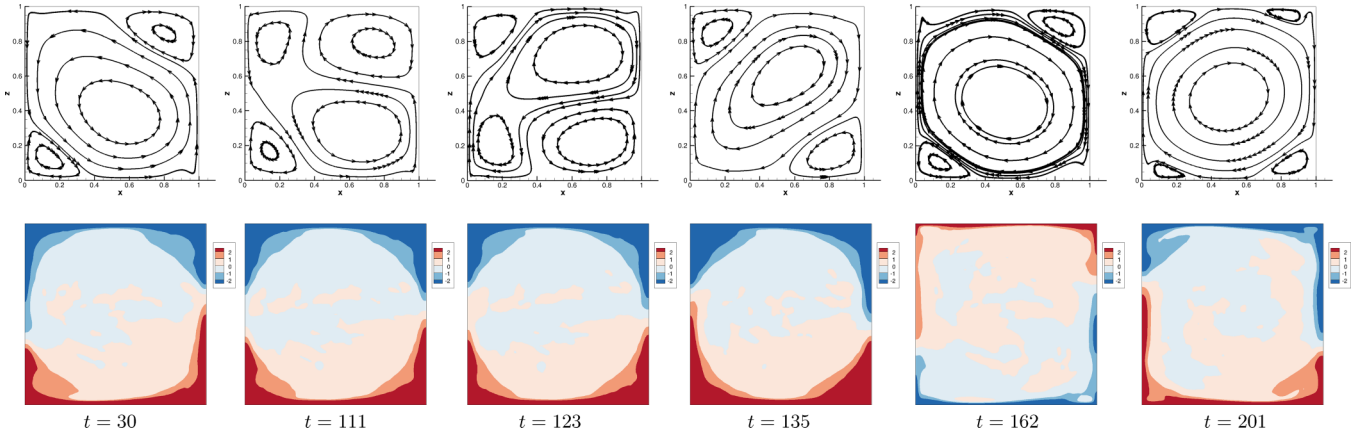

FIG. 6. Projected field from the DNS onto the first five POD modes at the same times as in Fig. 5. Top: velocity streamlines. Bottom: temperature contours 0.2, 0.15, 0.1, 0.05, −0.05, −0.1, −0.15, −0.2 (dashed lines indicate negative values).

TABLE IV. Values of the model coefficients.

c_1	c_2	c_3	c_4	c_5	c_6	c_7	c_8	c_9	c_{10}				
1.16	1.20	3.01	1.08	4.04	6.81	0.98	0.95	3.97	7.20				
α	χ	α'	χ'	β	μ	γ	ν	δ	δ'	ξ	ξ'	ϵ	ω
0.24	−0.26	0.12	0.06	24.12	15.31	0.10	0.05	0.035	0.0035	0.018	−0.44	0.035	0.018

plumes are being rotated about by the large-scale circulation independently from the horizontal boundary layers. The strong reorganization of the plumes indicates that smaller scales become important in the latter part of the reversal. As the flow reaches the quasistationary state at $t = 171$, the large-scale features of the full flow are again captured correctly by the projection. The dynamics of the flow can therefore be well described by the low-dimensional representation except for the latter part of the reversal.

IV. MODEL DYNAMICS

A. Model derivation

Following the approach described in [8], we derive a low-dimensional model by projecting the Navier-Stokes equations onto the first five spatial eigenfunctions, which capture 90% of the total energy. The general form of the model is

$$\dot{a}^n = L_{mn}a^m + Q_{mpn}a^m a^p + T_n, \tag{9}$$

where details of the model are given in the Appendix. The form of the model is obtained by computing the linear and quadratic coefficients (see Tables II and III) and retaining only the largest terms in the evolution equations. The effect of the unresolved scales is represented by modified linear and cubic coefficients. The model can thus be written as follows:

$$\dot{L} = (\chi - \alpha r^2)L + (\chi' - \alpha' r^2)L_* + c_1 LQ, \tag{10}$$

$$\dot{Q} = (\mu - \beta r^2)Q - c_2 L^2 - c_3 L L_* - c_4 S^2, \tag{11}$$

$$\dot{S} = (\nu - \gamma r^2)L + c_5 SQ + c_6 L S_* - c_7 L_* S_*, \tag{12}$$

$$\dot{L}_* = (\xi - \delta r^2)L_* + (\xi' - \delta' r^2)L + c_8 LQ, \tag{13}$$

$$\dot{S}_* = (\omega - \epsilon r^2)S_* - c_9 LS + c_{10} L_* S, \tag{14}$$

where

$$r = L^2 + Q^2 + L_*^2 + S^2 + S_*^2.$$

The coefficient c_i appearing in the evolution equation for mode a^n characterizes the interaction between modes a^p and a^q and is obtained from the quadratic coefficient Q_{nmp} using

$$c_i = Q_{nmp}\left(\frac{\lambda_p \lambda_p}{\lambda_n}\right)^{1/2}.$$

These quadratic coefficients constitute the nonadjustable parameters of the model. We checked that the selected quadratic terms are energy preserving, i.e., that

$$\frac{1}{c_1}\dot{L}L + \frac{1}{c_2}\dot{Q}Q + \frac{c_3}{c_8 c_2}\dot{L}_* L_* + \frac{c_4}{c_2 c_5}\dot{S}S + \frac{c_4 c_6}{c_2 c_5 c_9}\dot{S}_* S_* = 0.$$

This requires that $c_4 c_9 = c_{10} c_3$ which is verified within the precision with which the coefficients are computed.

The linear part of the model is characterized by a single off-diagonal term representing a coupling between the L and the L_* modes, which share the same symmetries. The (L, Q, L_*) subspace corresponding to centrosymmetry preserving modes is an invariant subspace of the model, while the modes S and S_* form a symmetry-breaking subspace. The two subspaces are coupled through the cubic feedback term and the quadratic interaction between mode S and mode Q. The model depends on 14 adjustable, linear, and cubic parameters. The value of the model coefficients used in the integration are given in Table IV.

B. Dynamical behavior of the model in the rotation-invariant subspace

We first study the dynamics of the model in the three-dimensional, centrosymmetric space, which remains invariant by the model equations. In the invariant subspace the equations are of the form

$$\dot{L} = (\chi - \alpha r^2)L + (\chi' - \alpha' r^2)L_* + c_1 LQ, \tag{15}$$

$$\dot{Q} = (\mu - \beta r^2)Q - c_2 L^2 - c_3 L L_*, \tag{16}$$

$$\dot{L}_* = (\xi - \delta r^2)L_* + (\xi' - \delta' r^2)L + c_8 LQ, \tag{17}$$

where

$$r = L^2 + Q^2 + L_*^2.$$

The parameters were adjusted so that the system admits two equilibria $(L^0, Q^0, -L_*^0)$ and $(-L^0, Q^0, L_*^0)$ corresponding to the quasistationary states observed in the simulation. L^0, Q^0, L_*^0 are taken equal to the rms of the corresponding POD mode eigenvalues. The linear cross-coupling α' between the L and L_* modes was found to be instrumental for the dynamics of the model. For lower values of $\alpha' < 0.11$, the equilibria are nodes. As α' increases, the nodes bifurcate to saddles and a heteroclinic cycle linking the two equilibria appears. The unstable manifold is one dimensional and located primarily along the L_* direction. However, the heteroclinic cycle rapidly bifurcates towards a robust limit cycle. The model therefore predicts reversals which occur in the absence of noise and involve only centrosymmetric modes. Other models have been shown to predict reversals in the absence of noise (for instance [12]) so this is not in itself a new result. The significant contribution brought here by the model is the idea that the centrosymmetric mode L_* plays a determinant role in reversals.

Histories of the POD amplitudes predicted by the model in the invariant subspace are illustrated in Fig. 7 and can be

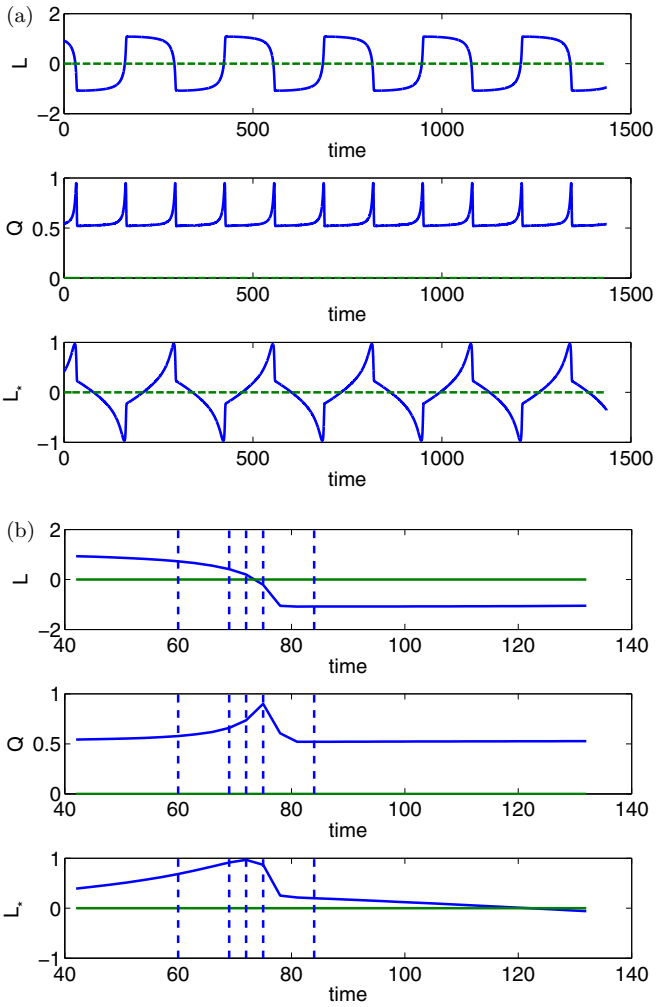

FIG. 7. (a) Evolution of the coefficients in the (L, Q, L_*) subspace; (b) blow-up during a single reversal event.

compared to the DNS values in Fig. 3(a). The model was integrated from an initial condition close to the quasistationary state in the DNS. Some similarity with the evolution of the DNS amplitudes is observed for the early part of the reversal, such as the increase in Q and the first sign switch and increase in L_* [compare Figs. 7(b) and 3]. We note in particular that $L_* > 0$ (respectively < 0) when L crosses the axis and becomes negative (respectively positive), which agrees with the observations made in Sec. III C. As mentioned previously, the agreement is not as good for the latter part of the reversal, which is dominated by small scales. However the quasisteady states, as well as the early part of the reversal, are all correctly captured by the model.

The process which initiates the reversal in the model physically corresponds to a deceleration of the wind coupling the boundary layer with the bulk. It is represented by the L_* mode, which is a centrosymmetric (nonsymmetry-breaking) mode. To illustrate this interaction between L_* and L, we represented the projection of the flow onto these two modes for different flow states in Fig. 8. We also represented the total heat transfer associated with the modes L, L_*, and Q for the same flow states in Fig. 9. Near a quasisteady state, L and L_* have opposite signs [Fig. 8(a)]. As mentioned before, this indicates that L_* reinforces the wind at the edges of the boundary layers associated with L. The roll fills out the cavity almost entirely. Figure 9(a) shows that the heat flux is maximal and almost constant in the vertical boundary layers (we recall that mode L contributes mostly in the center part, while the contribution of Q is predominant in the top and bottom parts).

As the intensity of mode L_* gradually decreases, it eventually switches sign, which corresponds physically to a deceleration, and eventually a reversal of the circulation in the upper edge of the layer, while creating motion in the opposite direction. The effect is to isolate the bulk region from the horizontal boundary layers, as can be seen in Fig. 8(b) for a value of $L_* = L_*^0$ (before the reversal starts) and Fig. 8(c) for $L_* = 2L_0$ (i.e., at the onset of reversal). As the intensity of L_* increases (with now the same sign as L), the large-scale circulation becomes more disconnected from the boundary layers. This disconnection has two consequences: On the one hand, a double shear layer of opposite sign ("squashed vortices") can be observed in Fig. 8(c). It isolates the roll from both horizontal layers and prevents efficient transport of thermal plumes originating there by creating a wind of opposite direction in the inner wall region, from which the opposite large-scale circulation will be able to grow. On the other hand, the roll encroachment on the vertical boundary layers is reduced, which inhibits the heat transfer between the bottom and the top of the cavity [Fig. 9(c)].

The physical process described above is observed in the simulation and is captured by the evolution equations of the model, which predict that the sign switch in L_* leads to the decrease of mode L, and its eventual collapse. In the model, reversals are therefore triggered by the decoupling of the boundary layers from the bulk, which in turn affects the heat transfer.

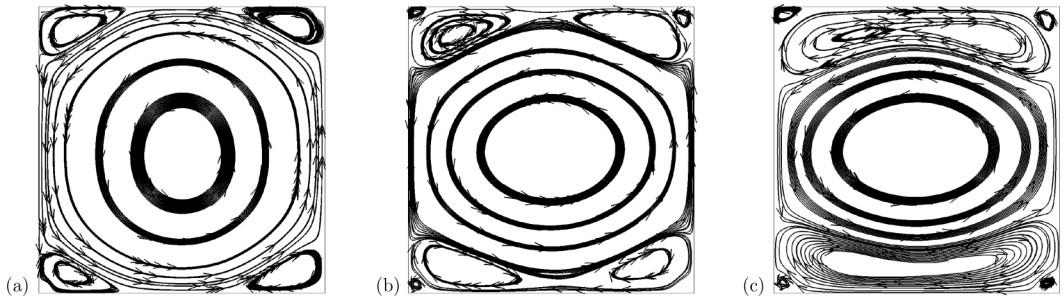

FIG. 8. Streamlines corresponding to a combination of the modes L and L_*; $L = L^0$; (a) $L_* = -L_*^0$, (b) $L_* = L_*^0$, (c) $L_* = 2L_*^0$.

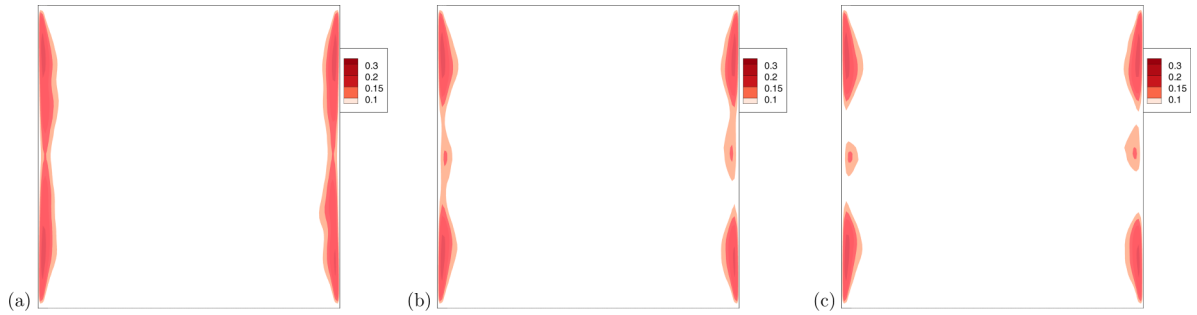

FIG. 9. Heat transfer associated with a combination of the modes L, Q, L_*: $L = L_0, Q = Q_0$; (a) $L_* = -L_*^0$, (b) $L_* = L_*^0$, (c) $L_* = 2L_*^0$.

The signature of the decoupling is given by the sign switch of L_*, which precedes the reversal (i.e., the sharp decrease and sign change of L) by a significant amount of time (the most probable value in the DNS is on the order of 40 convective units). The connection between the boundary layer and the bulk, which are two regions characterized by very different physical processes and scaling laws [24], appears therefore as a key player for the reversal dynamics of the model, and could be instrumental in triggering the reversals observed in the simulation.

A reconstruction of the fields corresponding to the single reversal depicted in Fig. 7(b) was carried out and is shown in Fig. 10 for the times identified by dashed lines in the histories of the coefficients. The dashed lines also respectively correspond to a sign change of L_*, a maximum of L_*, a zero value for L, a maximum of Q, and a value of L close to L^0. The quasistationary state at $t = 62$ corresponds to a main roll surrounded by two corner vortices. We observe that the center of the main roll shifts along the diagonal as it is squeezed along its main axis at $t = 72$. The corner rolls grow and develop (see at $t = 75$) into a quadrupolar flow. The vortices reconnect at $t = 78$ into a roll aligned on the opposite diagonal at $t = 81$. We note that the pinching of the main roll by the corner vortices occurs in a symmetric fashion since it occurs in the centrosymmetric subspace.

C. Influence of the symmmetry-breaking modes

We now examine how the presence of symmetry-breaking modes affects the dynamics of the model. We note that if these modes are set to zero in the model, they cannot grow since the other three form an invariant subspace. The centrosymmetric and the symmetry-breaking subspaces are coupled through a single quadratic term, through which S and Q exchange energy. The evolution equations for (S, S_*) read

$$\dot{S} = (\nu - \gamma r^2)S + c_5 SQ + (c_6 L - c_7 L_*)S_*, \tag{18}$$

$$\dot{S}_* = (\omega - \epsilon r^2)S_* - (c_9 L - c_{10} L_*)S. \tag{19}$$

Since the quadratic coefficients $c_i, i = 6,7,9,10$ are large and L and L_* have opposite signs near the equilibria, the off-diagonal terms are large and of opposite sign. This means that a strong oscillatory behavior should be expected for the symmetry-breaking modes. One can also show that in the absence of a coupling term, there cannot be a heteroclinic cycle in the (S, S_*) subspace and a nonzero equilibrium in that same subspace (which would correspond to cessations). The reason is as follows: for the equilibrium (L^0, Q^0, L_*^0) to be a saddle in the (S, S_*) subspace we need

$$(\nu - \gamma r^2)\left(\omega - \epsilon r_0^2\right) + (c_6 L - c_7 L_*)(c_{10} L - c_9 S_*) < 0,$$

where $r_0 = (L^0)^2 + (Q^0)^2 + (L_*^0)^2$. Since $c_6 L - c_7 L_*$ is proportional to $c_{10} L - c_9 S_*$, this requires $(\nu - \gamma r_0^2)$ and $(\omega - \epsilon r_0^2)$ to be large and of opposite sign. However, if there is a nonzero equilibrium in the symmetry-breaking subspace (S, S_*), then this equilibrium verifies

$$\nu - \gamma(S^2 + S_*^2) = \frac{\gamma}{\epsilon}[\omega - \epsilon(S^2 + S_*^2)] = 0,$$

which means that $\nu/\gamma = \omega/\epsilon$, which implies that $(\nu - \gamma r^2)$ and $(\omega - \epsilon r^2)$ cannot be of opposite signs. As a consequence there cannot be both one unstable and one stable direction in the symmetry-breaking subspace in the absence of a coupling term.

Integration of the model over a couple of reversals from an initial condition close to one of the quasistationary states is shown in Fig. 11. The behavior of the model in the centrosymmetric invariant subspace is similar to that of its

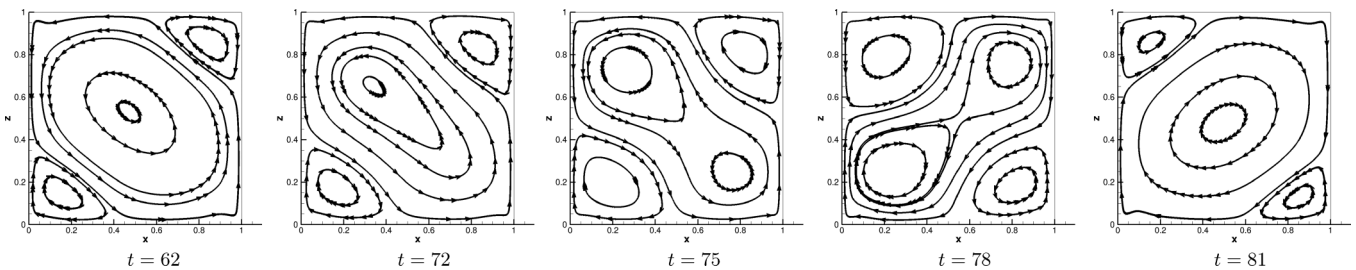

FIG. 10. Reconstructed field from the model in the centrosymmetric subspace modes at the times corresponding to the vertical lines in Fig. 7(b). Legend as in Fig. 6.

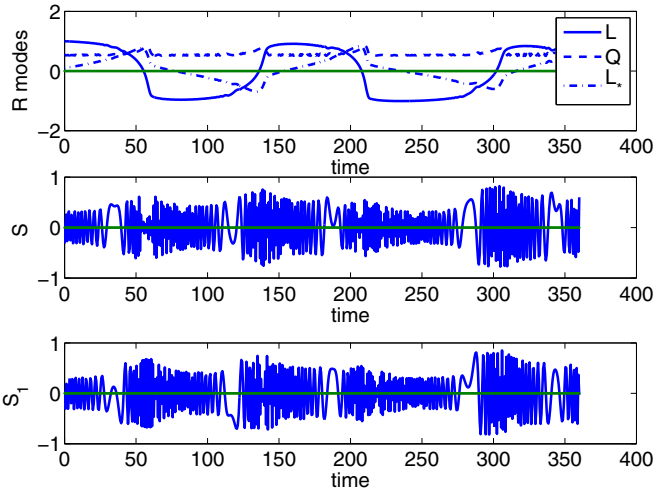

FIG. 11. Histories of the model in the full subspace.

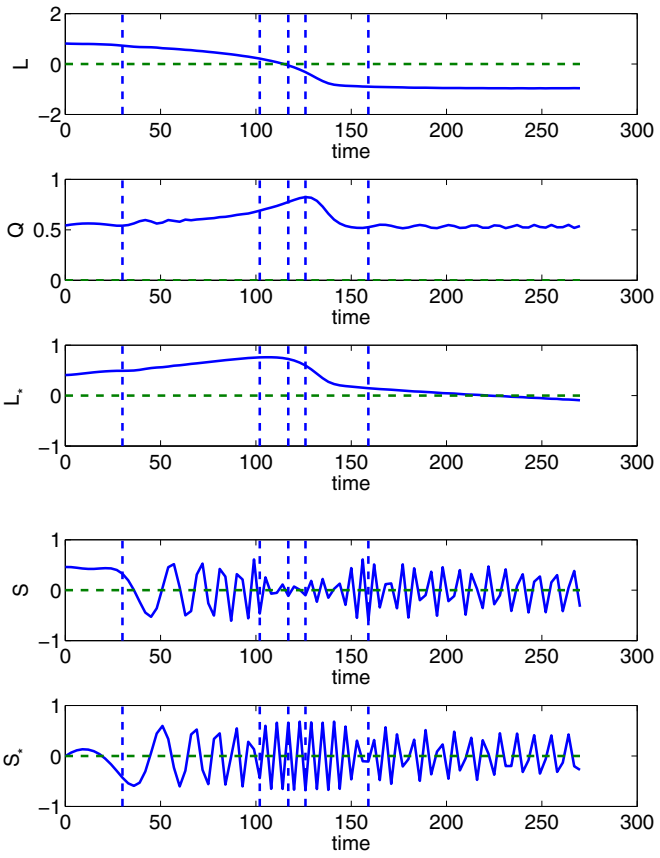

FIG. 12. Evolution of the coefficients in the full 5D model for a single reversal.

restriction to that subspace, which was studied in the previous section. The amplitudes of the symmetry-breaking modes S and S_* increase sharply during the reversal and roll collapse, in agreement with observations in the DNS [see Fig. 2(c)]. The high oscillation frequency of the modes is not observed in the DNS, which is presumably an effect of the truncation—a continuous range of high frequencies was observed in the DNS for mode S (results not shown here). However the mean amplitude of the symmetry-breaking modes in the model is close to the expected value from the DNS $\sqrt{\lambda_n}$: it is about 90% for mode S and about 180% for mode S_*. Reconstruction of fields during the single reversal event shown in Fig. 12 is plotted in Fig. 13 for selected times and displays the same sequence of events as in Figs. 6 and 10. The main roll apparent at $t = 33$ is squeezed in its middle part at $t = 105$. We can see that corner flows form either on the top or the bottom of the cell in an asymmetric manner which is closer to what is seen in the simulation (compare for instance Fig. 12 at $t = 105$ with Fig. 6 at $t = 111$ or $t = 93$). The quadrupolar flow is apparent at $t = 120$ and vortex reconnection takes place at $t = 129$. A new quasisteady state forms at $t = 162$. The main features of the reversal process are therefore captured by the model. The addition of symmetry-breaking modes results in more physically realistic reversals.

D. Time scales of the reversal

Essential characteristics of the dynamics are the duration and frequency of the reversals. The time between reversals $T_{\rm ir}$ is defined here as the time between two zeros of L and the duration of the reversal (also called transition time $T_{\rm tr}$) is defined as the time spent by L in the region $[-0.75L^0, 0.75L^0]$ where $\pm L^0$ are the quasisteady states. In addition, a new time scale corresponding to the time separating the disconnection of the core and boundary layer (sign switch of L_*) from the reversal (zero of L) can be defined. We will call it the precursor duration and denote it $T_{\rm prec}$. In the simulation, when more than one axis crossing took place (20% of the cases) $T_{\rm prec}$ was defined as the time between the first sign change of L_* when $LL_* < 0$ and the sign change of L. We found that the correlation between $T_{\rm prec}$ and $T_{\rm ir}$ was about 0.6 in the simulation, which supports the scenario of a limit cycle brought forth by the model. In contrast, there did not seem to be any strong correlation between $T_{\rm tr}$ and $T_{\rm rev}$ in the simulation. This suggests that the different stages of the reversal might be governed by different processes and is therefore consistent with the idea that small scales become important in the late part of the transition. The values reported in Table IV were chosen such that the period in the model without symmetry-breaking modes was found to be 130 time units, which is close to the period observed in the numerical simulation (about 110) and the transition time is 12 convective time units (in the simulation the mean and most probable value of the transition time are respectively 16 and 12 time units). The corresponding precursor duration was 85 units in the model (versus an average value of 73 in the simulation).

Figure 14 shows how the characteristic times of the model are modified when nonzero symmetry-breaking modes are included in the model. In the absence of these modes, for given values of the model coefficients, the period of the limit cycle is constant, so that the interreversal and transition times are fixed. When these modes are included, fluctuations are introduced in these time scales, as can be see in Fig. 14(a) for the transition time, which increases slightly, and in Fig. 14(b) for the interreversal period, which decreases down to 90 convective units. The precursor time scale [Fig. 14(c)] also decreases down to 60 convective units.

The evolutions of $T_{\rm tr}$, $T_{\rm ir}$, and $T_{\rm prec}$ are consistent with the idea that the effect of symmetry-breaking modes is

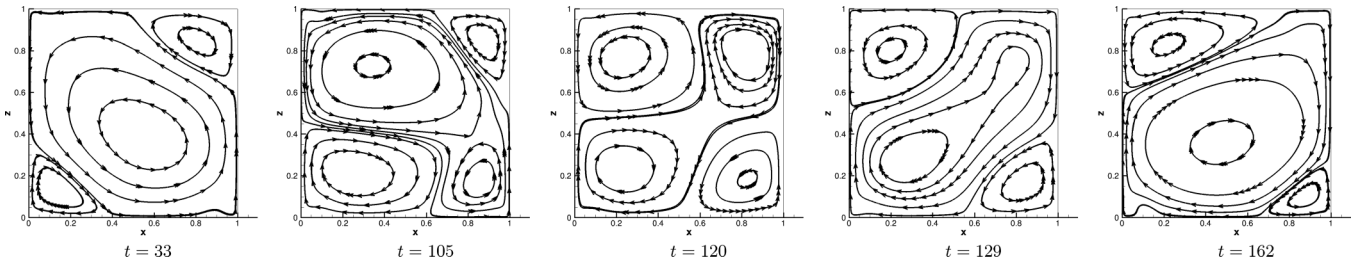

FIG. 13. Reconstructed field from the model in the full subspace at the times corresponding to the vertical lines in Fig. 12. Legend as in Fig. 6.

destabilizing. However the distribution spread of T_{ir} (and T_{prec}) is smaller than in the simulation, with respective standard deviation of 22 versus 74 convective time units in the simulation for T_{ir} and 13 against 63 convective units for T_{prec}, which again supports the idea that the distribution of the interreversal T_{ir} is influenced by small scales, which are not included explicitly in the model.

To account for the effect of unresolved small scales, Gaussian noise was introduced in the adjustable model coefficients which characterize the rate of small-scale energy extraction from the large scales. The statistics of the reversals were computed as follows: for a given noise level, a few thousand sets of coefficients were generated; the model corresponding to each set of coefficients was then integrated from an initial condition taken from the DNS in the centrosymmetric subspace over a time corresponding to several reversals. The mean and standard deviations of the transition and interreversal times are reported in Fig. 15 for different noise levels and can be compared to the values measured in the DNS (indicated as lines on the figure). Trends observed show some robustness with respect to the noise level. The mean transition time and its standard deviation $\sigma(T_{tr})$ tend to increase slightly with the noise level, which supports the idea that small scales have a destabilizing effect. The average interreversal period $\langle T_{ir}\rangle$ and precursor duration $\langle T_{prec}\rangle$ decrease as the noise level increases, which indicates that higher small-scale intermittency will tend to make reversals more frequent. For low noise levels, the standard deviation $\sigma(T_{ir})$ increases at first, but as the noise increases it decreases like $\langle T_{ir}\rangle$. For higher noise levels the average interreversal period and its standard deviation seem to converge towards equal values, as well as the precursor duration.

A good agreement with the DNS seems to correspond to a noise level of 5–15%, which is on the order of the energy fraction represented by the unresolved scales (10%). This is evidenced in Fig. 16 which compares the distributions of T_{tr}, T_{ir}, and T_{prec} for the model with a noise level of 10% with their counterparts in the simulation. We also represented in Figs. 16(d) and 16(e) (insets) the equivalent interreversal and transition times for standard reversals computed from the total angular momentum L_{2D}, which were respectively defined as (i) the time separating zeros of L_{2D} for the interreversal time, and (ii) the time during which $|L_{2D}|$ crossed the zero axis once and remained smaller than its maximum value by a standard deviation for the transition time.

Despite the crudeness of small-scale modeling, which assumes a separation between the resolved and unresolved scales, there is evidence of some statistical agreement, as the range of characteristic time scales found in the simulation is also present in the model. It is likely that more realistic modeling of the small scales could result in an even better statistical agreement, however this is outside the scope of the present paper.

V. DISCUSSION

In this section we discuss how our model represents the physics of the flow and we compare it with other models. As mentioned in the Introduction, several physically motivated models [5,9,12,13] have been proposed to describe reversals. These models are targeted at specific physical phenomena, which have been extracted from the full problem. For instance, Brown and Ahlers derived a model for the large-scale circulation in the cylinder using two physically motivated equations

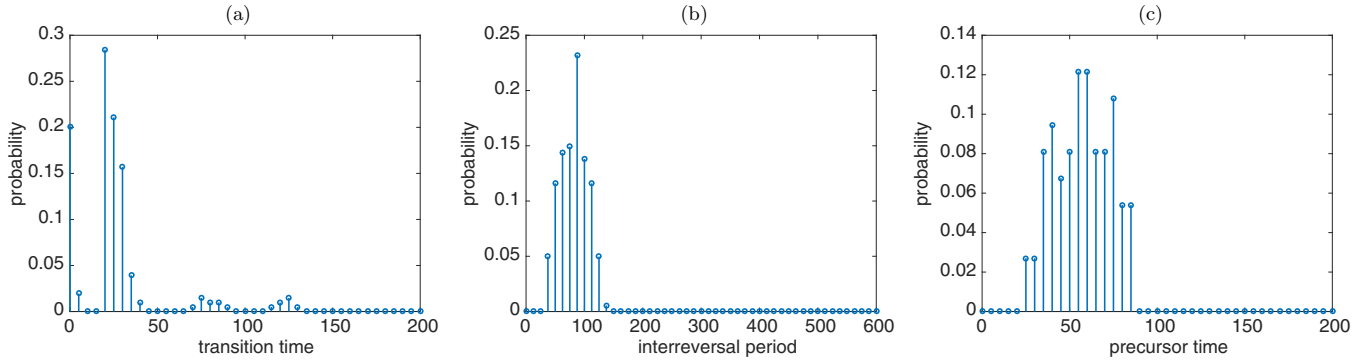

FIG. 14. Influence of the symmetry-breaking modes on the time scales of the reversal (a) transition time, (b) interreversal time, (c) precursor time.

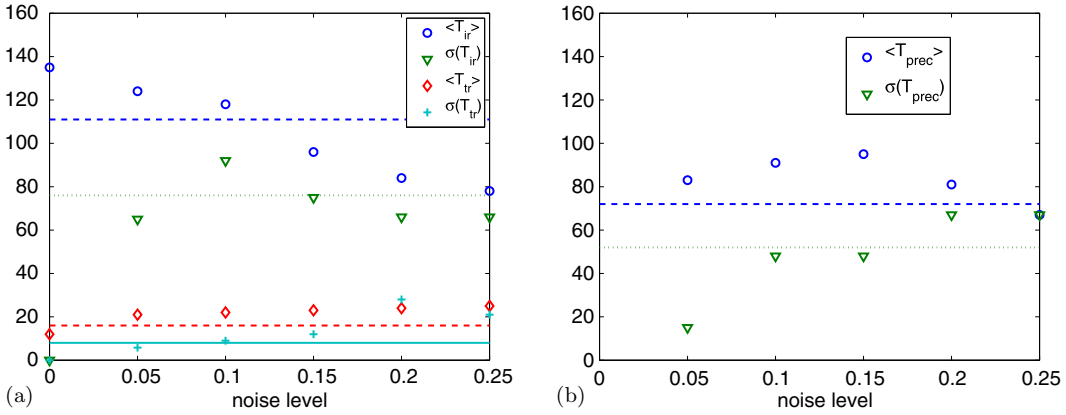

FIG. 15. (a) Evolution of the time scales as a function of the noise level. Dashed lines: mean values in the DNS; dotted line: standard deviation of T_{ir} in the DNS; solid line: standard deviation of T_{tr} in the DNS. (b) Evolution of the precursor time T_{prec}. Dashed line: mean value in the DNS; dotted line: standard deviation

for the strength and azimuthal component of the large-scale circulation. The model was able to reproduce cessations and rotations. Arujo *et al.* produced a three-dimensional model based on a deterministic balance between the drag and the buoyancy force to reproduce reversals. The form of their system is analogous to the Lorenz equations, with coefficients which can be made explicitly dependent on the Rayleigh and Prandtl numbers (via modeling of the Nusselt number). The model predicts the existence of reversals (regular or chaotic) depending on the value of these parameters.

As noted above, the evolution equations of these models are based on selected modeling of already identified physical phenomena. In contrast, our POD-based model is based on the extraction of a complete eigenfunction basis from empirical data and straightforward projection of the full Navier-Stokes equations onto this basis. As noted in the Introduction, these eigenfunctions are objective but artificial constructions which do not necessarily represent physical coherent structures of the flow. The POD-based model provides evolution equations for the amplitudes of the spatial eigenfunctions or modes. The first steps of the derivation of the (data-dependent) model do not therefore require any kind of *a priori* assumption about the problem: in particular, the procedure is entirely independent of the geometry or boundary conditions. We emphasize that

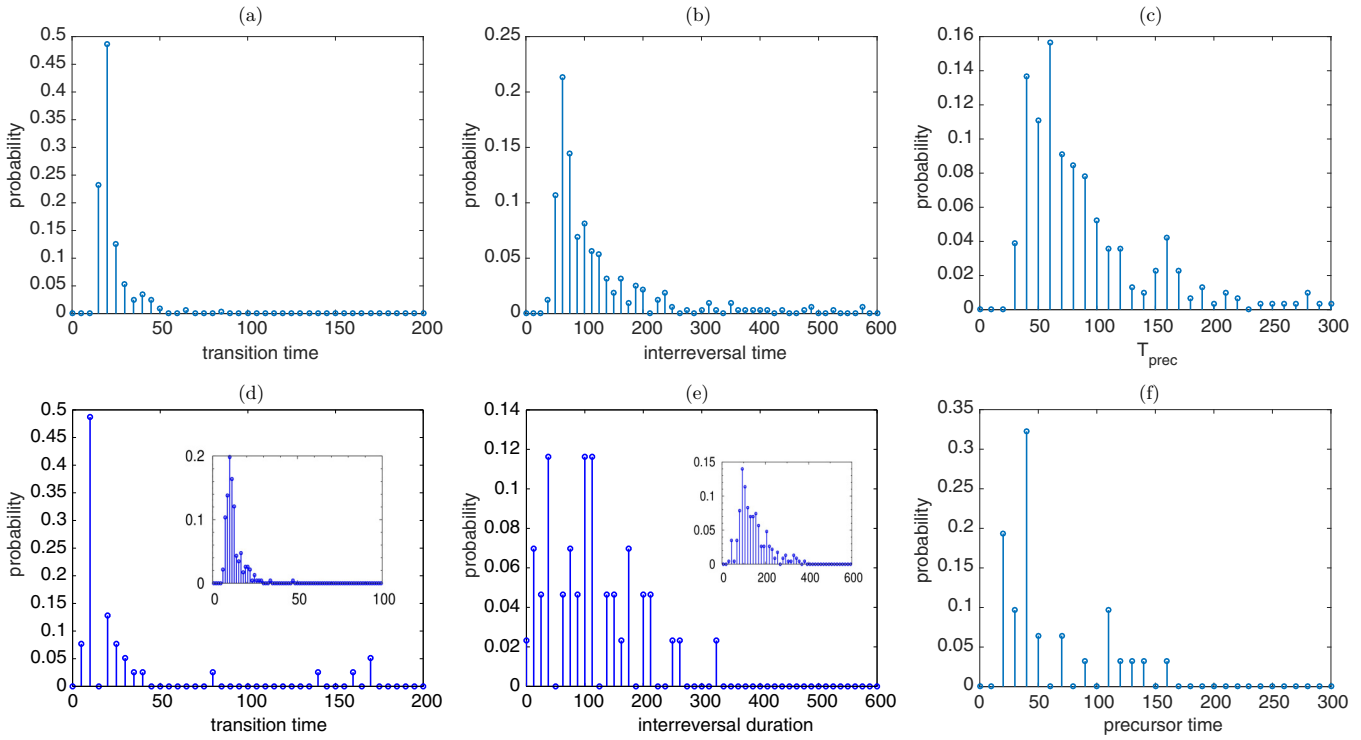

FIG. 16. Time scales of the reversals. Top row: model with a noise level of 10% in the coefficients: (a) transition time, (b) interreversal time, (c) precursor time. Bottom row: DNS: (d) transition time, (e) interreversal time, (f) precursor time—the inset pictures in (d) and (e) correspond to equivalent statistics performed on the global angular momentum L_{2D} over a time of 38 000 convective time units.

the POD eigenfunctions characterize the full problem, which can then be simplified by considering only the most energetic modes. Typically, these modes obey a set of symmetries which depend on the configuration considered. As pointed out by [19], mode symmetry constitutes a primary constraint for the temporal evolution of the mode amplitudes. In particular, the quadratic terms in the model characterizing the interactions between the amplitudes of the eigenfunctions are uniquely determined by the shape of these eigenfunctions and therefore reflect the specific symmetries of the POD modes associated with the configuration.

Approximations are required once a particular truncation has been chosen for the model. These approximations are the result of two processes: (i) the selection of the largest linear and quadratic coefficients, ensuring that the selection is compact yet consistent with pure redistribution of energy through the quadratic terms—which explains why the models corresponding to nested truncations will not be necessarily nested within each other; (ii) the addition of modified linear and cubic coefficients which represent the action of the unresolved scales (i.e., POD modes excluded from the truncation). Moreover, owing to symmetry, invariant subspaces may be found in the model: this is a key issue because of the constraints they induce for the dynamics of the modes. In particular, any trajectory originating in the invariant subspace will remain within this invariant subspace. This is not only of interest for a better understanding and possible further reduction of the dynamics, but also for control purposes.

To sum up, proper orthogonal decomposition provides objective identification of an energy-based hierarchy of flow patterns (POD eigenfunctions). Each truncation of any dimension can be associated with an interaction scenario for the relevant POD modes which attempts to model the physical processes occurring in the flow. The interaction scenarios depend on the symmetry and shape of the eigenfunctions retained in the truncations, and produce complementary representations of reversals. This provides a theoretically robust, unbiased framework where physical approximations in the model are reduced to the introduction of a closure scheme for the modes excluded from the truncation. However, the dependence of the eigenfunctions with respect to the configuration parameters is itself strongly implicit, which hampers the predictive capabilities of the models. Variations in the flow parameters (Rayleigh number, Prandtl number) are expected to lead to changes in the POD large-scale patterns, but are also likely to modify the action of the small scales on these patterns: additional modeling effort is therefore needed to extend the range of validity of the models.

In [8], we considered a three-mode truncation with modes L, Q, and S. The model is of the form

$$\dot{L} = (\chi - \alpha r^2)L + c_1 LQ, \tag{20}$$

$$\dot{Q} = (\mu - \beta r^2)L - c_2 L^2 + c_3 LS, \tag{21}$$

$$\dot{S} = (\nu - \gamma r^2)S + (\nu' - \gamma' r^2)L - c_4 LQ. \tag{22}$$

We note that, owing to a previous error, the signs in front of the coefficients c_1 and c_2 are opposite to those given in [8] (and consistent with those in the present model). No significant change in the dynamics was found when a comparison of this model with that described in [8] was carried out (for suitable small-scale parameters) and the conclusions of [8] were not modified. The model coefficients are given in Table V for the sake of completeness.

TABLE V. Values of the coefficients of the three-mode model [Eq. (22)].

$\tilde{c}_1$	$\tilde{c}_2$	$\tilde{c}_3$	$\tilde{c}_4$	χ	μ	ν	ν'	α	β	γ	γ'
1.22	1.25	0.51	0.27	−0.47	6.35	0.58	0.24	0.11	8.72	0.44	0.004

The dynamics of the 3D model consists of heteroclinic connections between fixed points. Fixed points are either of LQ type, i.e., they are close to the $S = 0$ plane and represent a quasisteady unique roll or of S type, i.e., they are close to the S axis and represent a two-roll mode. Both LQ- and S-type equilibria consist of nodes and saddles. Each heteroclinic connection linked a saddle of LQ type (respectively S type) to a node of S type (respectively LQ type). When the effect of unresolved scales is taken into account into the model by the addition of a random perturbation, the system can be kicked away from one of the nodes through random motion and reach the basin of attraction of the nearby saddle, from which it gets attracted towards another node, and so forth. The deterministic heteroclinic connections then form a noisy heteroclinic cycle linking all equilibria. It is important to note that noise is required to establish a dynamical connection between the two opposite large-scale circulations $\pm L^0$. The possibility of reversals in the 3D model is therefore conditioned on the presence of noise.

In contrast, with the five-mode model, creating the connection between the states $\pm L^0$ does not require explicit noise, but involves a new mode L_*. This mode is absent from the three-mode model, so there is no inconsistency between the two model predictions. The occurrence of reversals was found to depend on the intensity of the coupling between mode L and the additional mode L_*, which controls the connection between the boundary layer and the core region. Reversals correspond to the existence of a limit cycle in the invariant subspace (L, Q, L_*), close to an unstable heteroclinic cycle, and linking the quasisteady states $\pm L^0$. A change in the sign of the mode L_* is identified as a precursor for the reversal. The inclusion of modes S and S_* makes the time between reversals variable and on average shorter (just as in the 3D model, the S mode represents a direction of destabilization for the quasisteady states). The variability is still increased when random variations are allowed in the model coefficients.

Both 3D and 5D models predict reversals of the large-scale circulation in a consistent manner. At the onset of the reversal, all modes experience sharp variations: growth of the S mode is observed, while the quadrupolar mode Q collapses with the large-scale circulation L. The duration of the reversal as well as the mean period between reversals are found to match the times measured in the simulation when the effect of the unresolved modes is represented with additional model coefficients and noise perturbations. The mean time between reversals decreases as the noise level increases in the model. We note that the POD-based scenarios (which are by

construction global) are not inconsistent with the observations of Sugiyama *et al.* [20] who propose that the onset of reversal is associated with the local growth of corner flows (see Figs. 7 and 10). It is important to realize that the localized motions associated with the corner flows correspond to a mixture of many POD modes, so that direct comparison with Sugiyama's observations is not straightforward.

One major difference between the models is the addition of mode L_*, through which a direct connection between the states $\pm L^0$ can be established. The large-scale, deterministic part of the five-mode model captures the entire transition process, while only part of the transition could be reproduced in the three-mode model in the absence of noise. Moreover, it was shown that in the simulation, unlike other POD modes, mode L_* significantly varies between transitions, a behavior which is correctly captured by the five-mode model. This led to the definition of a precursor event as the first axis crossing of L_* following a reversal. The precursor event was successfully reproduced by the model, which supports the idea that reorganizations of the large-scale circulation in the simulation are not purely random occurrences, but could be part of a cycle reminiscent of the one displayed in the model. This opens up the possibility that reversals could be anticipated to some extent, and perhaps even controlled at the large-scale level, which is a new and enticing prospect brought about by the five-mode model.

VI. CONCLUSION

We have studied a new POD-based, five-mode model to represent the dynamics of the large-scale circulation in a 2D square Rayleigh-Bénard cell. It was shown that the large-scale description provided by POD is able to describe the velocity field at all times except during the latter part of the reversal.

The major result of this study is that a POD mode that becomes dynamically active before reversals was identified in the DNS. In particular, the mode changes sign between reversals, which we termed a precursor event. This event was correctly reproduced by the model and was found to be essential for the model reversal dynamics, which suggests that it could also be important for the reversals observed in the simulation. The effect of the sign change is to decelerate the wind in the region connecting the bulk and the boundary layers, limiting heat transfer between the top and bottom of the cavity. As a consequence, the main roll is isolated from the boundary layers, while a new shear layer of opposite sign is created in the horizontal boundary layers. A new time scale, which we call the precursor duration, can be defined: it corresponds to the interval between the precursor event and the onset of the reversal, and appears to be well correlated with the interreversal period in the simulation.

The model predicts excursions of the symmetry-breaking (noncentrosymmetric) modes during reversals, in agreement with the numerical simulation and the simpler, 3D model studied previously. The presence of symmetry-breaking modes in the model leads to fluctuations in the time scales of the reversal, but the amplitude of the fluctuations remains inferior to those of the simulation. However the agreement is significantly improved when noise representing small-scale intermittency is introduced in the model coefficients. The average transition time slightly increases, while the average interreversal period and precursor duration decrease with the noise level. This is consistent with the idea that higher small-scale intermittency will increase the likelihood of large-scale destabilization. The distributions of the characteristic time scales are found to agree relatively well with the DNS for noise levels of about 10%, which corresponds to the fraction of energy contained in the unresolved scales.

ACKNOWLEDGMENTS

This work was performed using HPC resources from CNRS (IDRIS-GENCI) (Grant No. 2013-2a0326). We thank J. Chergui and S. Xin for their assistance with the computations. We are very thankful to the referees for their helpful comments when revising the paper

APPENDIX: MODEL DERIVATION

The general form of the model is

$$\dot{a}^n = L_{mn}a^m + Q_{mpn}a^m a^p + T_n, \tag{A1}$$

where T_n represents the effect of the unresolved modes.

(i) Linear coefficients: The linear term L_{nm} contains a dissipative part L^d_{mn} and a buoyancy part L^b_{mn}, defined as

$$L^d_{mn} = \frac{1}{\mathrm{Ra}^{1/2}} \int \left(\mathrm{Pr}\nabla\underline{\phi}^n_{\underline{u}} : \left(\nabla\underline{\phi}^m_{\underline{u}}\right)^T + \nabla\phi^n_\theta \cdot \nabla\phi^m_\theta\right) d\underline{x}, \tag{A2}$$

where T represents the transposition operator, and

$$L^b_{mn} = \int (\phi^n_\theta \phi^m_w)\, d\underline{x} \tag{A3}$$

of the inner and outer sections of the large-scale circulation.

(ii) Quadratic coefficients: The quadratic terms Q_{mpn} (which cannot be confused with the quadrupolar mode Q) are defined as

$$\begin{aligned} Q_{mpn} = \int \big[&\left(\underline{\phi}^m_{\underline{u}} \cdot \nabla\underline{\phi}^p_{\underline{u}} + \underline{\phi}^p_{\underline{u}} \cdot \nabla\underline{\phi}^m_{\underline{u}}\right) \cdot \underline{\phi}^n_{\underline{u}} \\ &+ \left(\underline{\phi}^m_{\underline{u}} \cdot \nabla\underline{\phi}^p_\theta + \underline{\phi}^p_{\underline{u}} \cdot \nabla\phi^m_\theta\right)\phi^n_\theta\big] d\underline{x}. \end{aligned} \tag{A4}$$

They correspond to the transport of the Reynolds stress as well as that of the convective heat flux. The structure of the model is determined by the values of the largest quadratic coefficients.

Only one quadratic coupling term is retained between the invariant, centrosymmetric subspace and the symmetry-breaking subspace, in order to constitute the simplest model that provides quadratic coupling between the two subspaces.

(iii) Small-scale modeling T: Due to nonlinearity, unresolved modes appear in the model and need to be accounted for. In the absence of convection, the turbulent eddy viscosity is assumed to be proportional to the local strain rate s_{ij},

$$\nu_T \sim C|s_{ij}s_{ij}|^{1/2}.$$

This approximation is consistent with [25] which makes the case for a nonlinear subscale representation in low-dimensional models of the form

$$\nu_T \sim C'|k_<|^{1/2}, \tag{A5}$$

where $k_<$ represents the energy of the resolved modes a^n.

In the case of natural convection, a simple gradient diffusion hypothesis for the turbulent heat fluxes is generally not acceptable [26]. A better mode for the turbulent heat fluxes is given by [27]

$$\langle \theta u_i \rangle = -C_\theta \frac{k}{\epsilon} \langle u_i u_k \rangle \frac{\partial \langle \theta \rangle}{\partial x_k}, \tag{A6}$$

where k is the turbulent kinetic energy and ϵ is the dissipation. The evolution of the unresolved turbulent heat fluxes is therefore related to that of the unresolved turbulent stresses.

We generalize the approach of Osth *et al.* to thermal convection flows, using Eq. (A5), and we make one further simplification by expressing the fact that the temporal variations of the energy of the first POD modes are typically small compared to its mean value—the normalized standard deviation was less than 0.2 for the first five modes. Using

$$k(t) = \langle k \rangle + \tilde{k}(t)$$

with $|\tilde{k}(t)| \ll \langle k \rangle$, we can make the approximation

$$\sqrt{k(t)} = \sqrt{\langle k \rangle}[1 + \tilde{k}(t)/\langle k \rangle]^{1/2} \sim \sqrt{\langle k \rangle}\left(1 + \frac{1}{2}\frac{\tilde{k}(t)}{\langle k \rangle}\right)$$
$$= \frac{\sqrt{\langle k \rangle}}{2}\left(1 + \frac{k(t)}{\langle k \rangle}\right).$$

This leads to an affine representation for the eddy viscosity, which is in fact consistent with the optimal approach derived by [28] for transient flows. The eddy viscosity is therefore made up of a constant and a quadratic part, which yields linear terms and cubic terms in the equations. The cubic terms are taken to be positive to ensure global stability of the model.

[1] M. Berhanu, B. Gallet, R. Monchaux, M. Bourgoin, P. Odier, J.-F. Pinton, N. Plihon, R. Volk, S. Fauve, N. Mordant, F. Pétrélis, S. Aumatre, A. Chiffaudel, F. Daviaud, B. Dubrulle, and F. Ravelet, Bistability between a stationary and an oscillatory dynamo in a turbulent flow of liquid sodium, J. Fluid. Mech. **641**, 217 (2009).

[2] M. Grandemange, M. Gohlke, and O. Cadot, Turbulent wake past a three-dimensional blunt body. part 1 - global modes and bi-stability, J. Fluid Mech. **722**, 51 (2013).

[3] H. Xi and K. Xia, Flow mode transition in turbulent thermal convection, Phys. Fluids **20**, 055104 (2008).

[4] B. Podvin and A. Sergent, Proper orthogonal decomposition investigation of turbulent Rayleigh-Bénard convection in a rectangular cavity, Phys. Fluids **24**, 105106 (2012).

[5] E. Brown and G. Ahlers, Large-Scale Circulation Model for Turbulent Rayleigh-Bénard Convection, Phys. Rev. Lett. **98**, 134501 (2007).

[6] M. Chandra and M. Verma, Flow Reversals in Turbulent Convection Via Vortex Reconnections, Phys. Rev. Lett. **110**, 114503 (2013).

[7] J. Bailon-Cuba and J. Schumacher, Low-dimensional model of turbulent Rayleigh-Bénard convection in a cartesian cell with a square domain, Phys. Fluids **23**, 077101 (2011).

[8] B. Podvin and A. Sergent, A large-scale investigation of wind reversal in a square Rayleigh-Bénard cell, J. Fluid Mech. **766**, 172 (2015).

[9] K. Sreenivasan, A. Berdshadskii, and J. Niemelak, Mean wind and its reversal in thermal convection, Phys. Rev. E **65**, 056306 (2002).

[10] D. Molenaar, H. Clercx, and G. C. Heijst, Angular momentum of forced 2d turbulence in a square no-slip domain, Physica D **196**, 329 (2004).

[11] U. Frisch, *Turbulence: The legacy of A. N. Kolmogorov* (Cambridge University Press, Cambridge, England, 1995).

[12] F. Araujo, S. Grossmann, and D. Lohse, Wind Reversals in Turbulent Rayleigh-Bénard Convection, Phys. Rev. Lett. **95**, 084502 (2005).

[13] R. Benzi, Flow Reversal in a Simple Model of Turbulence, Phys. Rev. Lett. **95**, 024502 (2005).

[14] E. Brown and G. Ahlers, A model of diffusion in a potential well for the dynamics of the large-scale circulation in turbulent Rayleigh-Bénard convection, Phys. Fluids **20**, 075101 (2008).

[15] K. Bai, D. Ji, and E. Brown, Abiliy of a low-dimensional model to predict geometry-dependent dynamics of large-scale coherent structures in turbulence, Phys. Rev. E **93**, 023117 (2016).

[16] M. Chandra and M. Verma, Dynamics and symmetries of flow reversals in turbulent convection, Phys. Rev. E **83**, 067303 (2011).

[17] M. Verma, S. Ambhire, and A. Pandey, Flow reversals in turbulent convection with free-slip walls, Phys. Fluids **27**, 047102 (2015).

[18] D. Rempfer, On low-dimensional Galerkin models for fluid flow, Theor. Comput. Fluid Dyn. **14**, 75 (2000).

[19] P. Holmes, J. Lumley, and G. Berkooz, *Turbulence, Coherent Structures, Dynamical Systems and Symmetry* (Cambridge University Press, Cambridge, England, 1996).

[20] K. Sugiyama, R. Ni, R. Stevens, T. Chan, S.-Q. Zhou, H.-D. Xi, C. Sun, S. Grossmann, K.-Q. Xia, and D. Lohse, Flow Reversals in Thermally Driven Turbulence, Phys. Rev. Lett. **105**, 034503 (2010).

[21] K. Petschel, M. Wilczek, M. Breuer, R. Fredrich, and U. Hansen, Statistical analysis of global wind dynamics in vigorous Rayleigh-Bénard convection, Phys. Rev. E **84**, 026309 (2011).

[22] S. Xin, J. Chergui, and P. L. Quéré, 3D spectral parallel multi-domain computing for natural convection flows, *Parallel Computational Fluid Dynamics 2008*, Lecture Notes in Computational Science and Engineering, Vol. 74, edited by D. Tromeur-Dervout, G. Brenner, D. R. Emerson, and J. Erhel (Springer, Berlin, Heidelberg, 2010), pp. 163–171.

[23] L. Sirovich, Turbulence and the dynamics of coherent structures part i: Coherent structures, Q. Appl. Math. **45**, 561 (1987).

[24] S. Grossmann and D. Lohse, Scaling in thermal convection: A unifying theory, J. Fluid Mech. **407**, 27 (2000).

[25] J. Östh, B. R. Noack, S. Krajnović, D. Barros, and J. Borée, On the need for a nonlinear subscale turbulence term in POD models as exemplified for a high Reynolds number flow over an Ahmed body, J. Fluid Mech. **747**, 518 (2014).

[26] S. Choi and S. Kim, Turbulent modeling of natural convection in enclosures: A review, J. Mech. Science Technol. **26**, 283 (2012).

[27] N. Ince and B. Launder, On the computation of buoyancy-driven turbulent flows in rectangular enclosures, Int J. Heat Fluid Flow **10**, 110 (1989).

[28] B. Protas, B. Noack, and J. Osth, Optimal nonlinear eddy viscosity in Galerkin models of turbulent flows, J. Fluid Mech. **766**, 337 (2015).